Published in final edited form as:
Otol Neurotol. 2020 February ; 41(2): 277–284. doi:10.1097/MAO.0000000000002480.

3D-printed Microneedles Create Precise Perforations in Human Round Window Membrane *in situ*

Harry Chiang, BA[*], **Michelle Yu, BS**[*], **Aykut Aksit, MS**[†], **Wenbin Wang, MS**[†], **Sagit Stern-Shavit, MD**[*], **Jeffrey W. Kysar, PhD**[*,†,#], **Anil K. Lalwani, MD**[*,†,#]

[*]Department of Otolaryngology—Head and Neck Surgery, Columbia University Vagelos College of Physicians and Surgeons, New York, New York, U.S.A.

[†]Department of Mechanical Engineering, Columbia University, New York, New York, U.S.A.

Abstract

Hypothesis: 3D-printed microneedles can create precise holes on the scale of micrometers in the human round window membrane (HRWM).

Background: An intact round window membrane is a barrier to delivery of therapeutic and diagnostic agents into the inner ear. Microperforation of the guinea pig round window membrane has been shown to overcome this barrier by enhancing diffusion 35-fold. In humans, the challenge is to design a microneedle that can precisely perforate the thicker HRWM without damage.

Methods: Based on the thickness and mechanical properties of the HRWM, two microneedle designs were 3D-printed to perforate the HRWM from fresh frozen temporal bones *in situ* (n = 18 total perforations), simultaneously measuring force and displacement. Perforations were analyzed using confocal microscopy; microneedles were examined for deformity using scanning electron microscopy.

Results: HRWM thickness was determined to be 60.1 ± 14.6 (SD) μm. Microneedles separated the collagen fibers and created slit-shaped perforations with the major axis equal to the microneedle shaft diameter. Microneedles needed to be displaced only minimally after making initial contact with the RWM to create a complete perforation, thus avoiding damage to intracochlear structures. The microneedles were durable and intact after use.

Conclusion: 3D-printed microneedles can create precise perforations in the HRWM without damaging intracochlear structures. As such, they have many potential applications ranging from aspiration of cochlear fluids using a lumenized needle for diagnosis and creating portals for therapeutic delivery into the inner ear.

Keywords

Round window membrane; Human round window; Microneedle; Inner ear delivery; Perforation

---

Corresponding author: Anil K. Lalwani, MD, Division of Otology, Neurotology, and Skull Base Surgery, Department of Otolaryngology—Head and Neck Surgery, Columbia University College of Physicians and Surgeons, 180 Fort Washington Avenue, Harkness Pavilion, 8th Floor, New York, NY 10032, Phone: (212) 305-5820, anil.lalwani@columbia.edu.

[#]Co-Senior Authors

INTRODUCTION:

Intratympanic injection is an increasingly popular method of treatment for inner ear diseases because it allows for higher concentration of drug in the cochlea than would otherwise be tolerated with systemic administration (1–4). Intratympanic (IT) injection is not only limited to treatment, but has also been suggested for the diagnosis of inner ear disease using gadolinium-based contrast agents with magnetic resonance imaging and iodine contrast computed tomography (5–8). The success of these therapeutic and diagnostic procedures is contingent on reliable diffusion across the round window membrane. However, the permeability of the round window membrane (RWM) is highly variable and is significantly dependent on anatomic and physical characteristics such as thickness (9–10). In addition, the RWM thickness itself is variable and can depend on multiple factors including exposure to middle ear infection, toxins, or chemicals (11–13). As a result, IT injection to deliver therapeutic agents for the treatment of inner ear diseases such as Ménière's disease and sudden sensorineural hearing loss has been associated with variable clinical response and unpredictable side effects (14,15).

To overcome the physical barrier posed by the RWM, a variety of techniques, including microinjection, microperforation, microinfusion, and sustained drug release devices, have been investigated to enhance diffusion across the RWM (16–19). Over the last several years, our laboratory has focused on the development of microneedles to perforate the RWM for aspirating cochlear fluids for diagnosis and creating portals to enhance therapeutic diffusion into the inner ear (20–23). Using an *ex vivo* guinea pig model, we have demonstrated that a single microperforation representing 1% of the guinea pig RWM can increase the rate of diffusion more than 35-fold, greatly enhancing cochlear delivery in a time-efficient manner (19). In comparison to the guinea pig RWM, the human round window membrane is thought to be considerably thicker and the anatomy of the niche is more complex (24–26). Thus, the challenge of adapting this technology for human application requires designing microneedles that can safely and reliably perforate the thicker human round window membrane (HRWM): the microneedles need to be bigger and sturdier but just as sharp.

In this study, we investigate the efficacy of two microneedle prototypes—their designs based on the thickness and mechanical properties of the HRWM—to precisely perforate the HRWM with minimal membrane trauma and limited microneedle displacement to avoid intracochlear trauma (21). The efficacy of the microneedles is evaluated by measuring peak force of perforation, displacement of the microneedle during perforation, and size of perforation. These measurements were guided by clinical concerns: a small peak force is desired for minimizing membrane trauma, the distance traveled by the microneedle during perforation must be sufficiently small to avoid contact with structures behind the HRWM, and the size of perforations determines the precision of our microneedles.

MATERIALS AND METHODS:

Needle Design and Fabrication

Based on the thickness of the HRWM and previous characterizations of its mechanical properties, microneedles were designed to perforate the HRWM while minimizing trauma, membrane deformation, and intracochlear pressure (21). The designs were based on previous microneedle experiments in guinea pigs, which showed that perforation of the guinea pig RWM requires approximately 1 mN of force (23). As the HRWM is approximately 4–5x thicker than in the guinea pig, the microneedles designed for human use required a sturdier construction that resists microneedle bending or damage. Several design modifications were made to the previous microneedle design to compensate for the larger perforation force that was expected, as discussed below. Microneedles of two different shaft sizes were fabricated: 100 and 150 μm diameter. Microneedles of these sizes are thought to enhance drug diffusion across the HRWM while minimizing the potential for outward leakage of cochlear fluid (19). Each microneedle has a shaft height of 350 μm, which is larger than in guinea pig microneedles, to accommodate the deformation that the HRWM undergoes during perforation so the *hilt* of the microneedle does not contact the HRWM during perforation (Fig. 1). All microneedles have a shaft-to-tip taper angle of 60°, which is larger than in guinea pig microneedles, to prevent the microneedle from bending during perforation. The microneedle tips have a 5 μm radius of curvature, which is larger again for strength and stabilization (Fig. 1). The base of each microneedle was designed for mounting onto commercially available 30-gauge syringe needles (Industrial Unsterilized Blunt Tip Dispensing Needle with Luer Lock from BSTEAN, USA) with an inner diameter of 160 μm and outer diameter of 300 μm.

The microneedles were 3D-printed using two-photon polymerization (2PP) lithography with the Photonic Professional GT system (Nanoscribe GmbH, Karlsruhe, Germany). The substrate material was a crystal Si (100) wafer and the photoresist was IP-S (Nanoscribe GmbH) in a Dip-in Laser Lithography configuration with a 25x objective (Nanoscribe GmbH). Stereolithography files were generated using the SolidWorks (Dassault Systems SolidWorks Corporation, Concord, New Hampshire) computer aided design (CAD) software. These files were subsequently converted into Direct Laser Writing commands using the Describe (Nanoscribe GmbH) software. After completion of 2PP, the microneedles were rinsed in a propylene glycol monomethyl ether acetate solution and subsequently in two baths of isopropyl alcohol. At this point, the microneedles were ready for use, and were mounted onto the syringe needles with resin epoxy.

Tissue Preparation

Fresh, frozen human temporal bones were purchased from a commercial vendor (Science Care, Phoenix, Arizona). Samples were drilled in the Columbia University Department of Otolaryngology—Head & Neck Surgery Temporal Bone Surgical Dissection Lab. Six temporal bones (ages 62–74) were dissected to completely expose the HRWM from the middle and inner ear sides with the following steps: first, the cochlea was exposed with a canal wall down mastoidectomy and by opening the facial recess. The cochlea was removed from the surrounding temporal bone. Finally, the HRWM was isolated within a thin ring of bone and cleared of false membranous tissue and basilar membrane attachments. The prepared HRWMs were transported in phosphate buffered saline (PBS) and kept hydrated during all stages of experimentation.

Perforation of HRWM

The HRWMs were perforated three times each from the middle ear side, using same size microneedles within a HRWM. Three HRWMs were perforated with 100 µm microneedles, and the other three with 150 µm microneedles using an in-house microindenter setup (n = 18 perforations). Perforation locations depended on the surgical anatomy of each HRWM. The microindenter setup consists of a motorized linear translator to which the microneedle is secured (Zaber Technologies Inc., Vancouver, British Columbia, Canada) and a force transducer to measure the axial force exerted on the microneedle during perforation (Transducer Techniques, Temecula, California). For stabilization the HRWMs were bonded to plastic 3D-printed stages using dental cement. A 3D digital microscope (VHX-5000, Keyence Corporation of America, Elmwood Park, New Jersey) was used to visualize the experiments and capture videos, which were used to position the HRWMs in relation to the microneedles and to identify perforation events. The perforations were performed at room temperature at a prescribed rate of 150 µm/minute.

HRWM Confocal Microscopy

The HRWMs were imaged prior to perforation for overall structure and thickness and after perforation to inspect individual perforations. In preparation for imaging, the HRWMs were immersed in 1 mM Rhodamine B dissolved in PBS for 30 minutes, serially rinsed in PBS three times, and then soaked in PBS for 12 hours. Confocal imaging was performed using a Nikon A1R scanning confocal attachment on an Eclipse TiE microscope stand (Nikon Instruments, Melville, New York). Images of the entire HRWM were taken using a 10x/0.45 Plan Apo objective lens (Nikon) and required stitching (ImageJ-Fiji). Orthogonal slices were used to measure the thickness of the HRWM, with twenty-five measurements per HRWM, equally spaced in the orthogonal plane and the stacking direction (Fig. 2). To measure perforation sizes, images using a 20x/0.75 Plan Apo VC objective lens (Nikon) were projected in the stacking direction with maximum intensity to visualize a flattened membrane. Perforation sizes were measured manually and confirmed by scrolling through images slices in ImageJ-Fiji. If debris obstructed visualization of a perforation under fluorescence microscopy, transmitted white light was used instead. The areas of the perforations were measured by outlining each perforation and computing the area.

SEM of Microneedles

After perforating the HRWM, the microneedles were examined for potential bending and damage using scanning electron microscopy (Zeiss Sigma VP Scanning Electron Microscope).

Statistical Analysis

Statistical analysis was performed in MATLAB. Peak force and microneedle displacement are presented as median with interquartile range (IQR). Perforation dimensions are presented as their mean ± standard deviation (SD). Linear mixed effects models were used to compare measurements between the two microneedle sizes while accounting for intermembrane variability. The significance threshold was set at .05.

RESULTS:

HRWM Thickness

The thickness across all HRWMs, determined by confocal microscopy, was 60.1 ± 14.6 (SD) μm. Rhodamine B staining of the HRWM, which allows for visualization of the HRWM collagen and elastin tissue fibers, showed marked uniformity in the orientation of collagen and elastin fibers (Fig. 2A) (27).

Perforation Size and Shape

The microneedle perforations were slit-shaped with distinct major axes and minor axes (Fig. 3A). In all cases, the major axis aligned with the orientation of collagen and elastin fibers in the HRWM with the minor axis perpendicular to the fiber direction. Average dimensions of perforations created from each needle size are shown in Table 1 with standard deviation.

Note that the major axes of the perforations are approximately equal to the microneedle shaft diameters. During a perforation, an opening is created in the HRWM that is at least as large as the microneedle shaft diameter. After withdrawing the microneedle, the perforation partially closes along the minor axis while the major axis retains its length, resulting in the slit-shape. Although the major axis of the perforation is directly correlated with the diameter of the microneedle shaft, the relationship between microneedle diameter and perforation minor axis is less clear (Table 1). There was a significant difference in perforation minor axis between different microneedle shaft sizes ($p = .01$), as determined by a linear mixed effects model with perforation minor axis as a fixed effect and specific HRWM sample number as a random effect to account for intermembrane variability.

Microneedle Integrity

The used microneedles were indistinguishable from unused microneedles under light microscopy. SEM of the microneedles after perforation confirmed that the microneedles did not undergo notable deformation or damage; only the tips of the microneedles had minimal signs of blunting or bending after use (Fig. 3B).

Perforation Force Curves

A representative example of the force applied to the HRWM during microneedle indentation is illustrated in Figure 4 as a function of time and as a function of microneedle displacement, alongside a schematic of the relative microneedle and HRWM locations throughout perforation. Positive displacement indicates microneedle movement towards the HRWM. These force curves explain the events that occur during perforation. Upon microneedle contact with the HRWM (a), the force increases until a first peak (b) when the microneedle tip is about to perforate the membrane. The microneedle tip then perforates the membrane, indicated by the temporary drop in force (c). The force rises again to a second peak (d) as the microneedle taper expands the perforation to the size of the microneedle diameter. Immediately, the force drops due to slipping of the needle along the microneedle shaft, indicating a complete perforation, at which time the microneedle is withdrawn (e). The microneedle then encounters a negative force (f) due to friction between the membrane and the microneedle. Although individual experiments were associated with minor variations in the shape of the force curves, the majority followed the shape described in Figure 4. In what follows, *peak force* (d) is defined as the maximum force during a perforation, *trough force* (f) is the minimum (usually negative) force during perforation, and the *microneedle displacement* (g) is the distance that the microneedle travels during perforation, which can be obtained from the difference in microneedle positions between (d) and (a).

As detailed in the Methods section, each HRWM was perforated three times in different locations. There was no apparent difference in peak forces between one perforation and subsequent perforations, or peak forces from perforations at different locations within the same HRWM (see Supplemental Digital Content A, which describes statistical analyses and a comparison between consecutive force curves in the same HRWM).

Peak Force and Microneedle Displacement

The median peak force across all perforation experiments was 54 mN (IQR 46–71 mN). For 150 μm microneedles, the median peak force was 70 mN (IQR 34–72 mN). For 100 μm microneedles, the median was 53 mN (IQR 50–60 mN). The box-plot in Figure 5A shows the distribution of peak forces according to microneedle shaft size.

The median microneedle displacement across all perforation experiments was 257 μm (IQR 245–294 μm). For 150 μm microneedles, the median microneedle displacement was 294 μm (IQR 246–337 μm). For 100 μm microneedles, the median was 254 μm (IQR 247–264 μm). The box-plot in Figure 5B shows the distribution of microneedle displacement according to microneedle shaft size.

DISCUSSION:

This study presents two novel designs of 3D-printed microneedles for perforating the HRWM with the goal of enhancing diffusion of therapeutic and diagnostic agents into the inner ear. Both 100 and 150 μm microneedles created perforations with major axis equal to microneedle diameter and standard deviations representing less than 20% of the means. As such, the microneedles create both accurate and precise perforations. The relationship between microneedle diameter and the minor axis is more complex; the mean minor axis from 100 μm microneedles was less than half the size of those from 150 μm microneedles.

In comparison with guinea pig RWM perforations, the HRWM perforations were narrower than expected; whereas the perforations in guinea pigs were lens-shaped with the minor axes representing ~25% of the major axes, the perforations in HRWM were slit-shaped with minor axes representing 7–11% of the major axes (23). This finding suggests that the HRWM may be under higher tension than the guinea pig RWM, although further investigation into its mechanical properties is necessary. Previous efforts by our laboratory to model the round window membrane have shown that a membrane with uniformly oriented collagen and elastin fibers is stiffer than a membrane with randomly oriented fibers. The fibers in the HRWM appear to be more uniformly oriented than in the guinea pig RWM; this stiffness may be contributing to the slit-shape of the perforations. Moreover, the slit-shape suggests that the primary mechanism of HRWM perforation is fiber-fiber separation, rather than tearing of the HRWM. This is further supported by the observation that the collagen and elastin fibers remain continuous along the sides of the perforation without signs of damage. These findings are promising indicators for the ability of the HRWM to heal after perforation; *in vivo* studies will clarify the healing process of the round window membrane after microneedle perforation.

Consistent with expectations, the thicker HRWM and broader microneedle taper design required higher peak perforation forces compared to in guinea pig. There was no notable difference in the peak forces between 100 and 150 μm diameter microneedles, which suggests that shaft diameter alone does not account for peak force during perforation. Perhaps the radius of curvature of the microneedle tip or the taper angle of the microneedle tip play a role in determining the peak force. These insights are important for further improving microneedle design. Importantly, SEM of the microneedles post-perforation show that the microneedles are durable and can withstand at least the peak forces measured in this study.

Of note, the peak perforation forces showed a wider data spread with the 150 μm diameter microneedles compared to the 100 μm microneedles. This may be explained, in part, by considering the HRWM as a chain mail, where the ability of the HRWM to resist breaking is dependent on its weakest link. Although a larger microneedle may theoretically require a larger force to perforate the HRWM, it also recruits and samples a larger area in the HRWM, and thus has a higher chance of encountering a weak link. For these reasons, a larger microneedle is likely to be associated with greater data spread than a smaller microneedle of similar design.

The sharp tip of the microneedles succeeded in reducing membrane deformation during perforation. Membrane deformation during perforation is important because large deformations may increase risk of unintentional trauma to the HRWM. Moreover, large membrane deformations can decrease intracochlear volume and thus increase intracochlear pressure during the perforation process. In the microneedle force curves, the decrease in force after the first peak and before the second peak indicates the release of elastic strain energy in the HRWM induced by the initial perforation by the microneedle tip. Afterwards, the microneedle glides through the HRWM, expanding the size of the perforation laterally. During the lateral expansion of the perforation (second peak), friction between the HRWM and the microneedle contributes to further deformation of the HRWM in the direction of microneedle movement (axial). This is in contrast to perforations using blunt-tip needles (no taper to the tip), in which we expect single-peaked force curves (28). With a blunt needle, the membrane deforms continuously from initial needle contact until complete perforation when the entire needle diameter passes through the HRWM. Membrane relaxation does not occur until after complete perforation—thus, all aspects of a blunt needle perforation contribute to deformation of the HRWM. In comparison, the microneedles in this study induce less HRWM deformation and minimize increases in intracochlear pressure associated with microneedle perforation.

The microneedle displacement that occurs during perforation was also studied to ensure that the distance that the microneedle travels is less than the available space behind the HRWM. The distance between the HRWM and the basilar membrane—the nearest structure within the inner ear—is approximately 1.2 mm (21,29). Across all perforation experiments, even the maximum microneedle displacement was less than half the distance that is available behind the HRWM. There was no notable difference in microneedle displacement between 100 and 150 μm microneedles. Both microneedles, regardless of shaft diameter, thus show promise as surgical tools that can safely create perforations in the HRWM without damaging inner ear structures.

The microneedles described in this study are designed to create perforations in the HRWM that may enhance drug diffusion into the cochlea for the treatment of inner ear diseases. The next step—to fabricate hollow, or lumenized microneedles—will explore the potential applications of microneedles as diagnostic and therapeutic tools via direct aspiration of cochlear fluid and direct injection of therapy. Although these microneedles are currently envisioned for used in the operating room, the long-term goal of this project is to design and develop microneedles for minimally invasive office-based procedures. Recent advances in the development of microendoscopes and mini-otoscopes have demonstrated access to the RWM via transtympanic approach (30,31). The availability of in-office visualization of the HRWM would greatly facilitate future applications of microneedles for the practicing otolaryngologist.

Supplementary Material

Refer to Web version on PubMed Central for supplementary material.

Acknowledgements:

The authors gratefully acknowledge support by the National Institutes of Health (NIH) National Institute on Deafness and Other Communication Disorders (NIDCD) with award number R01DC014547. The authors also thank Jimmy K. Duong for statistics consultation, Miguel Arriaga and Elizabeth S. Olson for experiment consultation, Theresa C. Swayne and Emilia L. Munteaunu for assistance with microscopy, and the Columbia University Department of Otolaryngology—Head and Neck Surgery for granting use of the Temporal Bone Surgical Dissection Lab. Imaging was performed in the Confocal and Specialized Microscopy Shared Resource of the Herbert Irving Comprehensive Cancer Center at Columbia University, supported by NIH grant #P30 CA013696 (National Cancer Institute). The confocal microscope was supported by NIH grant #S10 RR025686.

Conflicts of Interest and Source of Funding:

Research was funded by the National Institutes of Health (NIH) National Institute on Deafness and Other Communication Disorders (NIDCD) with award number R01DC014547. Dr. Anil K. Lalwani is on the Medical Advisory Board of Advanced Bionics. For the remaining authors, no conflicts of interest were declared.

REFERENCES:

1. Silverstein H, Lewis WB, Jackson LE, Rosenberg SI, Thompson JH, Hoffmann KK. Changing trends in the surgical treatment of Ménière’s disease: results of a 10-year survey. Ear Nose Throat J. 2003;82: 185–7, 191–4. [PubMed: 12696238]
2. Diamond C, O’Connell DA, Hornig JD, Liu R. Systematic review of intratympanic gentamicin in Meniere’s disease. J Otolaryngol. 2003;32: 351–361. [PubMed: 14967079]
3. Slattery WH, Fisher LM, Iqbal Z, Friedman RA, Liu N. Intratympanic steroid injection for treatment of idiopathic sudden hearing loss. Otolaryngol Head Neck Surg. 2005;133: 251–259. [PubMed: 16087024]
4. Bird PA, Begg EJ, Zhang M, Keast AT, Murray DP, Balkany TJ. Intratympanic versus intravenous delivery of methylprednisolone to cochlear perilymph. Otol Neurotol. 2007;28: 1124–1130. [PubMed: 18043438]

5. Abt NB, Lehar M, Guajardo CT, et al. Intratympanic Iodine Contrast Injection Diffuses Across the Round Window Membrane Allowing for Perilymphatic CT Volume Acquisition Imaging. Otol Neurotol. 2016;37: 403–407. [PubMed: 26859543]
6. Pyykkö I, Zou J, Poe D, Nakashima T, Naganawa S. Magnetic Resonance Imaging of the Inner Ear in Meniere’s Disease. Otolaryngol Clin North Am. 2010;43: 1059–1080. [PubMed: 20713245]
7. Nakashima T, Naganawa S, Sugiura M, et al. Visualization of endolymphatic hydrops in patients with Meniere’s disease. Laryngoscope. 2007;117: 415–420. [PubMed: 17279053]
8. Wesseler A, Óvári A, Javorkova A, Kwiatkowski A, Meyer JE, Kivelitz DE. Diagnostic Value of the Magnetic Resonance Imaging With Intratympanic Gadolinium Administration (IT-Gd MRI) Versus Audio-Vestibular Tests in Menière’s Disease: IT-Gd MRI Makes the Difference. Otol Neurotol. 2019;40: e225–e232. [PubMed: 30550412]
9. Yoshioka M, Naganawa S, Sone M, Nakata S, Teranishi M, Nakashima T. Individual differences in the permeability of the round window: evaluating the movement of intratympanic gadolinium into the inner ear. Otol Neurotol. 2009;30: 645–648. [PubMed: 19415042]
10. Goycoolea MV. Clinical aspects of round window membrane permeability under normal and pathological conditions. Acta Otolaryngol. 2001;121: 437–447. [PubMed: 11508501]
11. Yoda S, Cureoglu S, Shimizu S, et al. Round window membrane in Ménière’s disease: a human temporal bone study. Otol Neurotol. 2011;32: 147–151. [PubMed: 21131881]
12. Sahni RS, Paparella MM, Schachern PA, Goycoolea MV, Le CT. Thickness of the human round window membrane in different forms of otitis media. Arch Otolaryngol Head Neck Surg. 1987;113: 630–634. [PubMed: 3566946]
13. Nordang L, Linder B, Anniko M. Morphologic changes in round window membrane after topical hydrocortisone and dexamethasone treatment. Otol Neurotol. 2003;24: 339–343. [PubMed: 12621354]
14. Marin E, Perez N. Hearing loss after intratympanic gentamicin therapy for unilateral Ménière’s Disease. Otol Neurotol. 2003;24: 800–806. [PubMed: 14501459]
15. Bremer HG, Rooy IV, Pullens B, et al. Intratympanic gentamicin treatment for Ménière’s disease: a double-blind, placebo-controlled trial on dose efficacy - results of a prematurely ended study. Trials 2014;15: 328. [PubMed: 25135244]
16. Salt AN, Hartsock J, Plontke S, LeBel C, Piu F. Distribution of dexamethasone and preservation of inner ear function following intratympanic delivery of a gel-based formulation. Audiol Neurootol. 2011;16: 323–335. [PubMed: 21178339]
17. Park SH, Moon IS. Round window membrane vibration may increase the effect of intratympanic dexamethasone injection. Laryngoscope. 2014;124: 1444–1451. [PubMed: 24155116]
18. Mikulec AA, Hartsock JJ, Salt AN. Permeability of the round window membrane is influenced by the composition of applied drug solutions and by common surgical procedures. Otol Neurotol. 2008;29: 1020–1026. [PubMed: 18758387]
19. Kelso CM, Watanabe H, Wazen JM, et al. Microperforations significantly enhance diffusion across round window membrane. Otol Neurotol. 2015;36: 694–700. [PubMed: 25310125]
20. Stevens JP, Watanabe H Kysar JW, Lalwani AK. Serrated needle design facilitates precise round window membrane perforation. J Biomed Mater Res A. 2016;104: 1633–1637. [PubMed: 26914984]
21. Watanabe H, Cardoso L, Lalwani AK, Kysar JW. A dual wedge microneedle for sampling of perilymph solution via round window membrane. Biomed Microdevices. 2016;18. doi:10.1007/s10544-016-0046-2 [PubMed: 26846875]
22. Wazen JM, Stevens JP, Watanabe H, Kysar JW, Lalwani AK. Silver/silver chloride microneedles can detect penetration through the round window membrane. J Biomed Mater Res B Appl Biomater. 2017;105: 307–3011. [PubMed: 26506512]
23. Aksit A, Arteaga DN, Arriaga M, et al. In-vitro perforation of the round window membrane via direct 3-D printed microneedles. Biomed Microdevices. 2018;20: 47. [PubMed: 29884927]
24. Fujita T, Shin JE, Cunnane M, et al. Surgical Anatomy of the Human Round Window Region: Implication for Cochlear Endoscopy Through the External Auditory Canal. Otol Neurotol. 2016;37: 1189–1194. [PubMed: 27228017]

25. Carpenter AM, Muchow D, Goycoolea MV. Ultrastructural studies of the human round window membrane. Arch Otolaryngol Head Neck Surg. 1989;115: 585–590. [PubMed: 2706104]
26. Watanabe H, Kysar JW, Lalwani AK. Microanatomic analysis of the round window membrane by white light interferometry and microcomputed tomography for mechanical amplification. Otol Neurotol. 2014;35: 672–678. [PubMed: 24622022]
27. Shelley WB. Fluorescent staining of elastic tissue with Rhodamine B and related xanthene dyes. Histochemie. 1969;20: 244–249. [PubMed: 4190306]
28. Nguyen CT, Thang Nguyen C, Vu-Khanh T, Dolez PI, Lara J. Puncture of elastomer membranes by medical needles. Part I: Mechanisms [Internet]. International Journal of Fracture. 2009. pp. 75–81. doi:10.1007/s10704-009-9326-7
29. Paprocki A, Biskup B, Kozłowska K, Kuniszyk A, Bien D, Niemczyk K. The topographical anatomy of the round window and related structures for the purpose of cochlear implant surgery. Folia Morphol. 2004;63: 309–312.
30. Plontke SK. Evaluation of the round window niche before local drug delivery to the inner ear using a new mini-otoscope. Otol Neurotol. 2011;32: 183–185. [PubMed: 21192347]
31. Za Mood, Daniel SJ. Use of a microendoscope for transtympanic drug delivery to the round window membrane in chinchillas. Otol Neurotol. 2012;33: 1292–1296. [PubMed: 22918111]

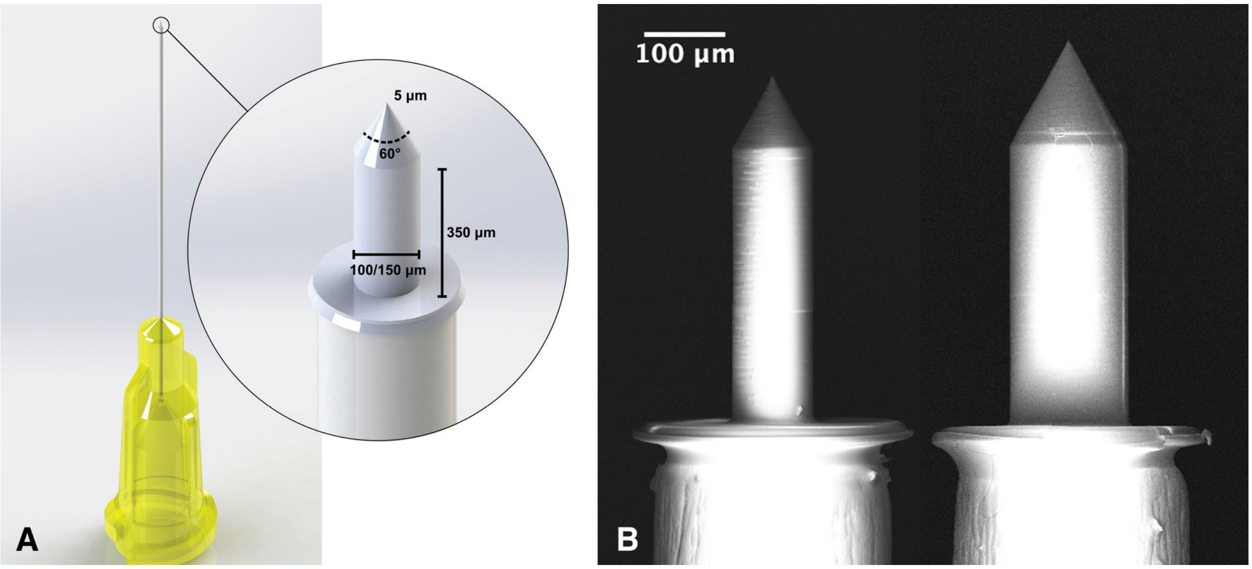

FIG. 1.

Microneedle design. *A*, a computer-aided design (CAD) schematic showing a microneedle mounted onto a 30-gauge syringe needle. Each microneedle has a shaft height of 350 µm and a 60° taper from the shaft to the tip, which has a 5 µm radius of curvature. *B*, a scanning electron microscopy (SEM) image of a 100 and 150 µm diameter microneedle side by side, both mounted onto 30-gauge syringe needles. The hilt is the flat portion of the microneedle that contacts the syringe needle.

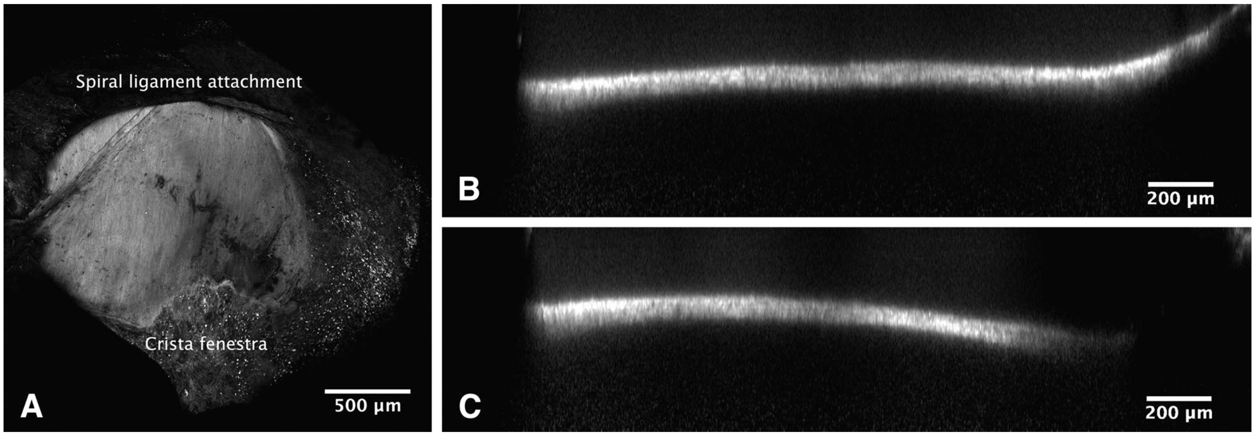

FIG. 2.

Confocal microscopy of a human round window membrane (HRWM) stained with Rhodamine B. *A*, a maximum intensity projection along the z-axis (into the page), viewed from the inner ear side; note the uniformity in collagen and elastin fiber orientation (running top to bottom). The crista fenestra, a bony crest at the anteroinferior edge of the round window, was frequently used as a landmark for orienting images. The dark areas result from out of focus debris casting shadows in the image. *B* and *C*, two cross-sections through a HRWM in different locations. Orthogonal views such as these were used for measuring the HRWM thickness.

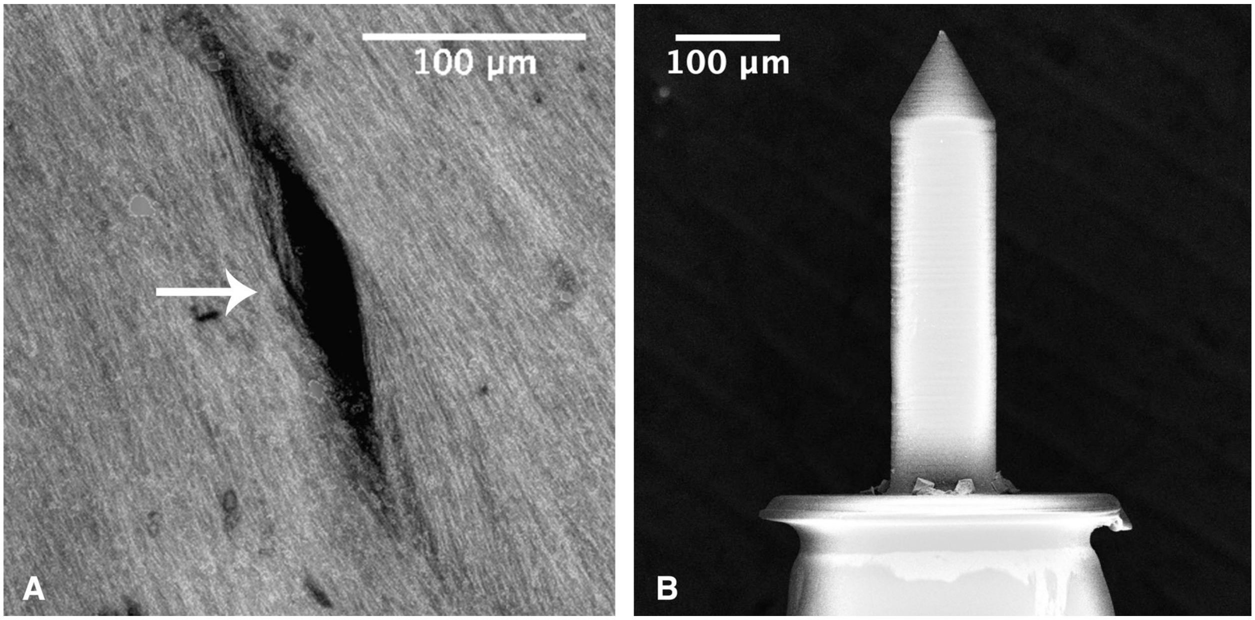

FIG. 3.

A, One 150 μm microneedle perforations (white arrow) visualized using a maximum intensity projection of confocal microscopy images. The perforation measurements were based solely on completely black areas and did not include areas that had noticeable enhancement. Collagen and elastin fibers appear continuous along the boundaries of the perforation. *B*, Scanning electron microscopy image (SEM) of a representative microneedle after perforation, which shows minimal signs of blunting and bending at the tip, and is otherwise indistinguishable from unused microneedles.

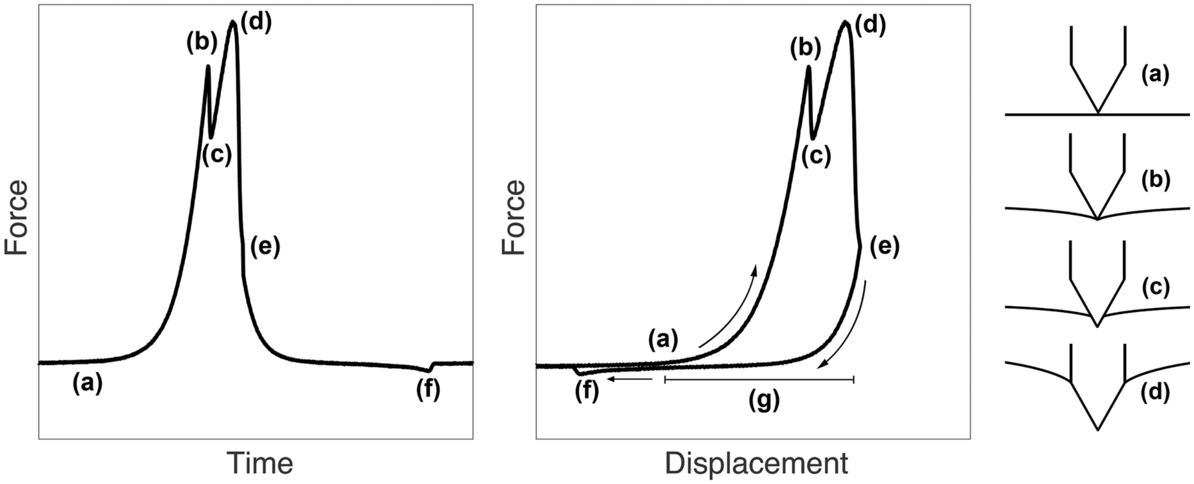

FIG. 4.

Force on the human round window membrane (HRWM) during microneedle perforation as a function of time. The microneedle contacts the HRWM at (a) and the measured force begins to increase. The first peak at (b) and subsequent drop (c) correspond to the microneedle tip perforation and the second larger local peak (d) corresponds to the full microneedle diameter perforation. This larger peak (d) is considered to be the *peak force* during a perforation. Subsequently there is a sharp drop to baseline and the microneedle is withdrawn (e). As the microneedle withdraws, it encounters a period of negative force due to friction between the membrane and the microneedle until the *trough force* (f). Finally the force reaches baseline. The *microneedle displacement* during perforation—the distance that the microneedle travels during perforation—is the interval (g), defined by the difference in microneedle position at event (d) and event (a).

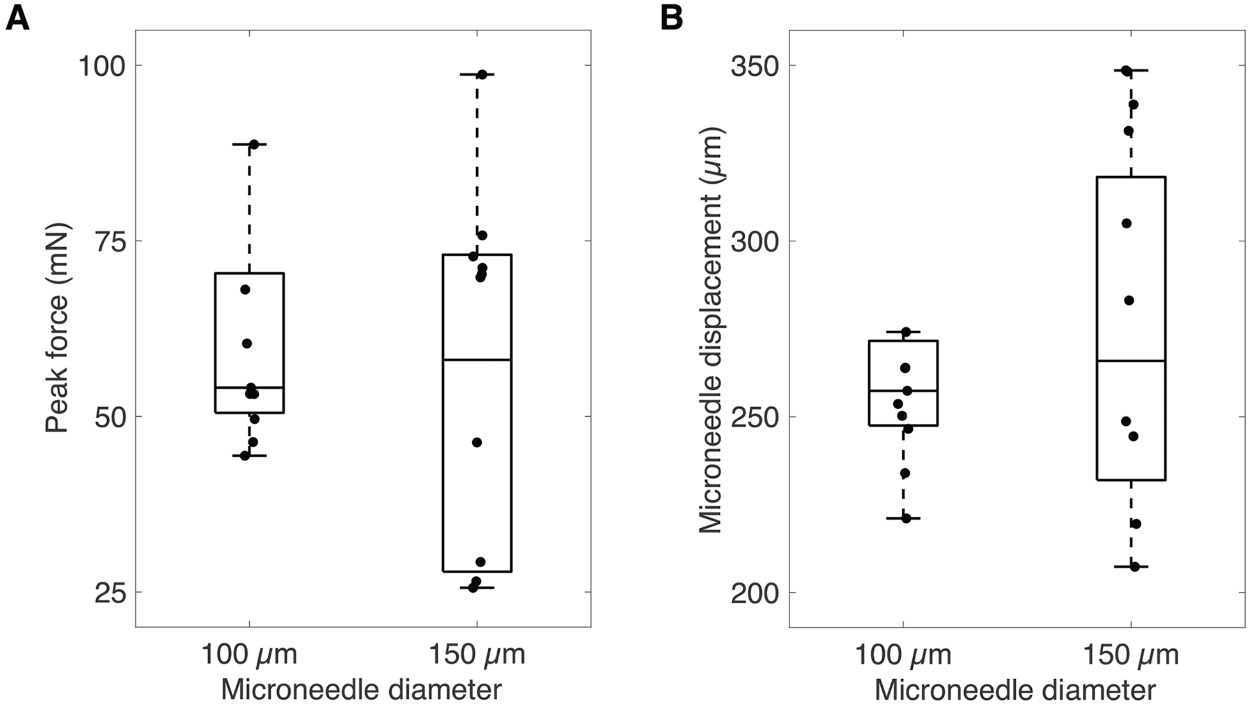

FIG. 5.

Box-plot of peak force (*A*) and microneedle displacement (*B*) during perforation for 150 and 100 μm microneedles, shown with raw data.

TABLE 1.

Perforation dimensions by microneedle shaft diameter

Microneedle Size (μm)	Major Axis (μm)	Minor Axis (μm)	Area (μm^2)
150	153.9 ± 20.9	15.9 ± 7.9	1865.8 ± 1235.6
100	103.4 ± 17.1	7.7 ± 2.6	705.2 ± 187.7